Research Article

Mechanical Characteristics of Tailings in Different Depositional Zones: A Case Study of Caijiagou Tailings Pond in Shaanxi, China

Longfei Zhang [iD],[1] **Zaiqiang Hu** [iD],[1] **Hongru Li** [iD],[1] **Haicheng She** [iD],[2,3] **Qiuxiang Qin** [iD],[4] and **Xiaoliang Wang** [iD][1]

[1]*Institute of Geotechnical Engineering, Xi'an University of Technology, Xi'an 710048, China*
[2]*School of Urban Construction, Yangtze University, Jingzhou 434032, China*
[3]*Key Laboratory of Reservoir and Dam Safety Ministry of Water Resources, Nanjing 210024, China*
[4]*Xi'an Engineering Investigation and Design Research Institute of China National Nonferrous Metals Industry Co. Ltd., Xi'an 710054, China*

Correspondence should be addressed to Zaiqiang Hu; huzq@xaut.edu.cn

This study examines the widespread practice of upstream tailings dam construction in metallurgical mines in China, conducting comprehensive testing and research on tailings from various depositional zones of the Caijiagou tailings pond. Analysis of the test results from three types of tailings reveals a systematic relationship between the mechanical characteristics of tailings and their depositional zones: the farther from the dam, the finer the tailings particles, categorized as silty clay tailing, silt tailing, and sandy silt tailing. Consistent patterns were observed in the consolidated-drained shear strength and consolidated-undrained effective shear strength of these tailings. Among these, sandy silt tailing exhibited the highest strength, whereas silty clay tailing displayed the lowest. The dynamic stress–strain relationships of all three tailings types are described using the Hardin equivalent viscous-elastic model, where the initial dynamic shear modulus and the maximum dynamic shear stress in the model increased with effective confining pressure. The damping ratios exhibited a three-stage trend with increasing dynamic strain: gradual increase, rapid growth, and then gradual stabilization. Under various consolidated stress conditions, the ratio of the damping ratio to the maximum damping ratio versus the reduction in dynamic shear modulus showed a favorable linear relationship. Under vibration conditions, the dynamic shear stress corresponding to tailings failure increased with higher effective confining pressure and consolidated stress ratio. Finally, this study summarizes the parameters and indicators related to the saturated tailings of iron mines used in the research. Our work provides a foundation and reference for the design of tailings dams and the development and utilization of abandoned tailings ponds.

1. Introduction

Tailings, the residual materials from ore processing during mining operations, are typically discharged as a slurry via pipelines or channels [1, 2]. The construction method of tailings dams influences whether tailings deposit within the pond or integrate into the dam structure [3–5]. In upstream tailings dam construction, cyclones often separate tailings sands and fines: the sands are utilized in dam construction, while the fines, governed by hydraulic principles and gravity,

settle within the pond. The engineering properties of tailings materials vary significantly across different depositional zones, profoundly impacting tailings dams' safety and stability [6]. The International Commission on Large Dams reports about 18,000 tailings dams globally, with incidents at these dams occurring twice as frequently as those at other dam types [7, 8]. Tailings ponds, containing various heavy metals and substantial amounts of sulfides, chlorides, cyanides, and other residual beneficiation reagents, pose severe environmental risks in the event of dam failures [9, 10]. Thus, addressing the

stability of tailings dams is crucial for sustainable development and responsible mining practices.

During natural deposition, the particle size distribution of tailings varies along the slope due to factors like ore beneficiation techniques, dam slope ratio, slurry concentration, and discharge rate [11–13]. Near the discharge outlet, in the dry beach area, tailings particles are coarser, while they are finer in the sedimentation area farther away. Due to their particle size distribution, tailings materials have a highly sensitive and unstable structure compared to natural soils, leading to significant differences in their static and dynamic behaviors [14–16]. Tailings sands, with larger pores, lower density, and lower plasticity index, are less weathered and altered, making them prone to liquefaction and strength loss under dynamic loading [17–19]. The dynamic behavior of tailings fines directly affects the seismic response and stability of tailings dams. Under commonly used seismic load levels in current engineering design, tailings fines reduce the seismic acceleration response of the dam, differing notably from the response of earth-rock dams in hydraulic engineering [20–22]. A correct understanding of tailings material properties is fundamental to analyzing tailings dam stability. Researchers have studied the mechanical properties of tailings materials, exploring the effects of mineral types [23], production processes [24], and deposition methods [25, 26] on their sedimentation and mechanical properties. Achievements in the static mechanical properties of tailings materials are more prominent. For example, some studies have discussed constitutive models for the static behavior of tailings materials [27, 28]. In terms of dynamic properties, studies have explored constitutive models and dynamic strength [29, 30], focusing on seismic safety characteristics of tailings clay and analyzing the influence of clay content and plasticity index on dynamic strength and pore pressure [31, 32]. Compared with natural soils, the nonuniformity of tailings materials is more pronounced, making research more complex. For instance, studies comparing cohesive soils and tailings fines have investigated the effects of mineral composition on liquefaction and residual deformation characteristics [33, 34]. However, research related to tailings materials is still limited compared to natural soils, especially in liquefaction identification and dynamic stability analysis. Our study innovatively examines the dynamic properties of tailings, particularly how variations in different depositional zones affect their dynamic behavior. For example, Wang et al. [35] conducted an experimental study on the dynamic characteristics of tailings with different reconsolidation degrees after liquefaction, providing significant insights into this aspect. Our research aims to expand upon this knowledge by systematically analyzing the dynamic test results of tailings from various depositional zones and exploring the relationship between these characteristics and the tailings' depositional areas.

Given the significant spatial variability in tailings, when subjected to static and dynamic loads, the mechanical characteristics and behaviors of tailings in different regions typically exhibit variations. Therefore, a detailed and in-depth investigation of specific tailings characteristics is crucial in the context of tailings dam engineering stability analysis.
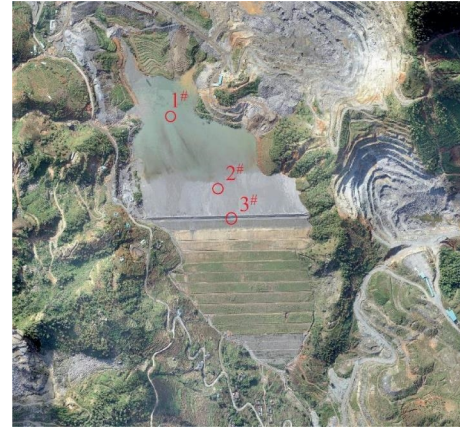

FIGURE 1: Location of tailings sampling.

This study focuses on tailings from three distinct areas in Shaanxi Province. From a geotechnical perspective, we extensively examined the particle size distribution and fundamental physical properties of the test samples. Static and dynamic tests were conducted to analyze the mechanical differences among tailings from different areas.

2. Experimental Materials and Methods

2.1. Experimental Materials. The experimental tailings were sourced from the Caijiagou Iron Mine tailings pond in Zhashui County, Shaanxi Province, as depicted in Figure 1. Among these, the fine tailings designated as $1^{\#}$ were from the sedimentation area, while $2^{\#}$ and $3^{\#}$ tailings were gathered from the dry beach and embankment areas, respectively. The $1^{\#}$ tailings, in a saturated state, exhibited a fine and loose texture. Conversely, the $2^{\#}$ and $3^{\#}$ tailings, originating from the dry beach and embankment, were notably denser, with tangible particle presence upon handling. Table 1 displays the physical characteristics of these three undisturbed sample groups. Specifically, $1^{\#}$ tailings contained 17.8% fines (0.05–0.002 mm) and 35.5% clay particles (<0.002 mm). In contrast, $2^{\#}$ tailings comprised 16.6% fines with a clay content of 16.4%, and $3^{\#}$ tailings had 14% fines and 10.6% clay. Figure 2 illustrates the particle size distribution curves for these samples. Based on liquid limit test results and particle size distribution analysis, the $1^{\#}$, $2^{\#}$, and $3^{\#}$ samples were categorized as silty clay tailing, silt tailing, and sandy silt tailing, respectively.

2.2. Experimental Methods. In this study, we adopted a comprehensive experimental plan to analyze the static and dynamic properties of tailings, integrating various test types and equipment (as shown in Figure 3). This approach included compression tests, triaxial shear tests, and dynamic tests. For specific test schemes, please refer to Table 2.

3. Static Characteristics of Tailings

3.1. Compressibility Characteristics. The results of the consolidation tests for the three types of tailings samples are shown in Figure 4. It can be observed that finer tailings

TABLE 1: Physical parameters of different iron tailings.

Sample number	Type	Specific gravity (G_s)	Dry density (g/cm^3)	Void ratio (e)	Plastic limit W_P (%)	Plastic limit W_L (%)	Plasticity index (I_p)
1#	Silty clay tailing	3.14	1.35	1.33	35.2	16.5	18.7
2#	Silt tailing	3.18	1.58	1.01	25.1	15.2	9.9
3#	Sandy silt tailing	3.25	1.71	0.90	20.5	11.4	9.1
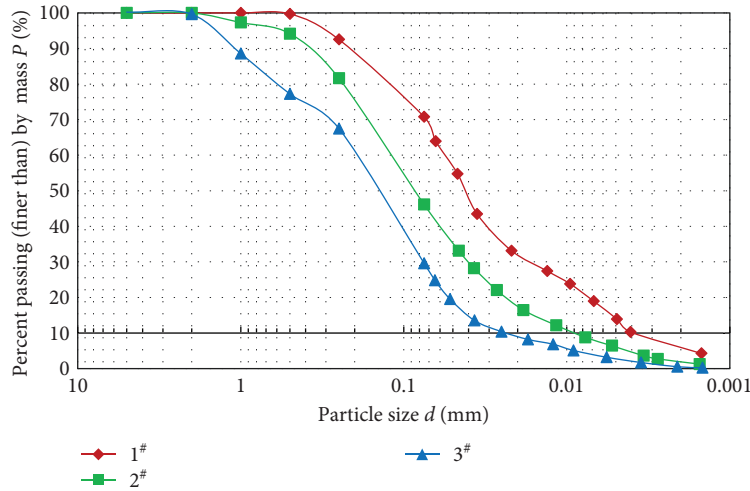
FIGURE 2: Grading curve of tailings.

(a)   (b)   (c)

FIGURE 3: (a) Single lever soil consolidation instrument, (b) strain-controlled direct shear instrument, and (c) dynamic triaxial testing instrument.

particles and larger initial void ratios are associated with stronger compressibility in the samples of naturally deposited tailings. Figure 5 illustrates the relationship between the compressibility coefficient and vertical pressure. From this graph, it can be concluded that for the same type of tailings, as the vertical pressure increases, the compressibility coefficient of the tailings specimens gradually decreases.

3.2. Shear Characteristics. In analyzing the shear strength of tailings, we focus on the role of normal stress acting on particles, as guided by the principle of effective stress. This principle states that the total stress on saturated tailings is a combination of pore water pressure and stress borne by the particles themselves—the latter being the effective stress. In our study, it's this effective stress that primarily determines

TABLE 2: Comprehensive experimental plan for tailings characterization.

Type of test	Equipment	Sample size	Conditions	Purpose
Compression tests	Single lever soil consolidation instrument (Figure 3(a))	Cylindrical, base area 50 cm^2, height 2 cm	Double-sided drainage, vertical pressures of 12.5, 25, 50, 100, 200, 400, 800, and 1,600 kPa	Investigate the compression deformation patterns of tailings and understand the impact of composition and gradation on the compression behavior of tailings
Triaxial shear tests	Strain-controlled direct shear instrument (Figure 3(b))	Cylindrical, base area 30 cm^2, height 2 cm	Two drainage methods, consolidated drained (CD) and undrained (CU), effective confining pressures of 50, 100, 200, and 300 kPa	Explore the shear strength of tailings, considering particle size, gradation, and drainage conditions, and the behavior of tailings under different vertical pressures
Dynamic tests	Dynamic tests (Figure 3(c)).	Cylindrical, base area 12 cm^2, height 80 mm	Consolidated-undrained cyclic triaxial tests, K_c set to 1.0 and 2.0, effective confining pressures set at 200, 400, and 600 kPa	Study the dynamic response of tailings under cyclic loading, including dynamic elastic modulus and damping ratio, and the dynamic shear stress value under a certain number of vibration cycles
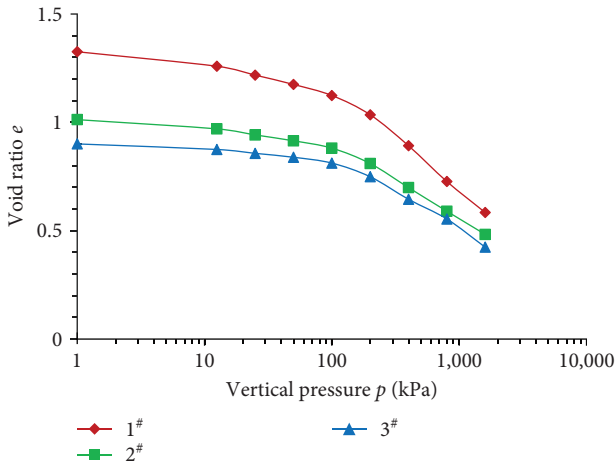
FIGURE 4: Compression curve of tailings in the e-lgp coordinate system.

FIGURE 5: Relation between compressibility coefficient and vertical pressure.

the shear strength of the tailings samples. Emphasizing this aspect allows us to better understand the specific behaviors and characteristics of the tailings in our research.

3.2.1. Consolidated-Drained Triaxial Shear Test. In this study, the strength parameters of tailings were evaluated through consolidated-drained triaxial shear tests. As depicted in Figure 6, various levels of confining pressures, specifically 50, 100, 200, and 300 kPa, were applied during the tests. The stress–strain curves indicate notable observations. The curves for samples 1# and 2# show similar trends, with an increase in confining pressure leading to a gradual rise in peak shear stress. At a confining pressure of 400 kPa, both sample sets exhibit characteristics of slight hardening. In contrast, sample 3# displays a clear softening behavior at
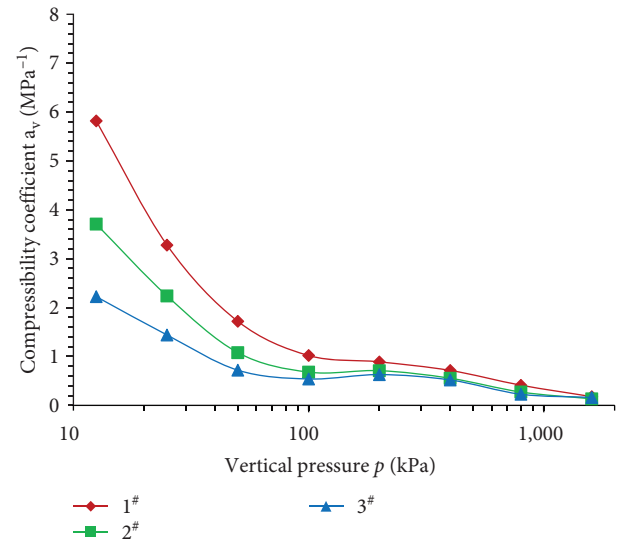
lower confining pressures, which diminishes as the confining pressure increases and vanishes at higher pressures.

3.2.2. Consolidation-Undrained Triaxial Shear Test. The test results for the three types of tailings samples are presented in Figures 7–9. In undrained tests, the volume of the tailings sample remains nearly unchanged when it reaches the critical void ratio (e_{cr}); under these conditions, no excess pore water pressure is generated. However, if the void ratio exceeds e_{cr} under consolidation pressure, the excess pore water pressure (u) generated upon sample failure could reduce the effective confining pressure (σ'_3).

Concerning the behavior of the different tailings samples, the stress–strain curve of sample 1# (a silty clay tailing,
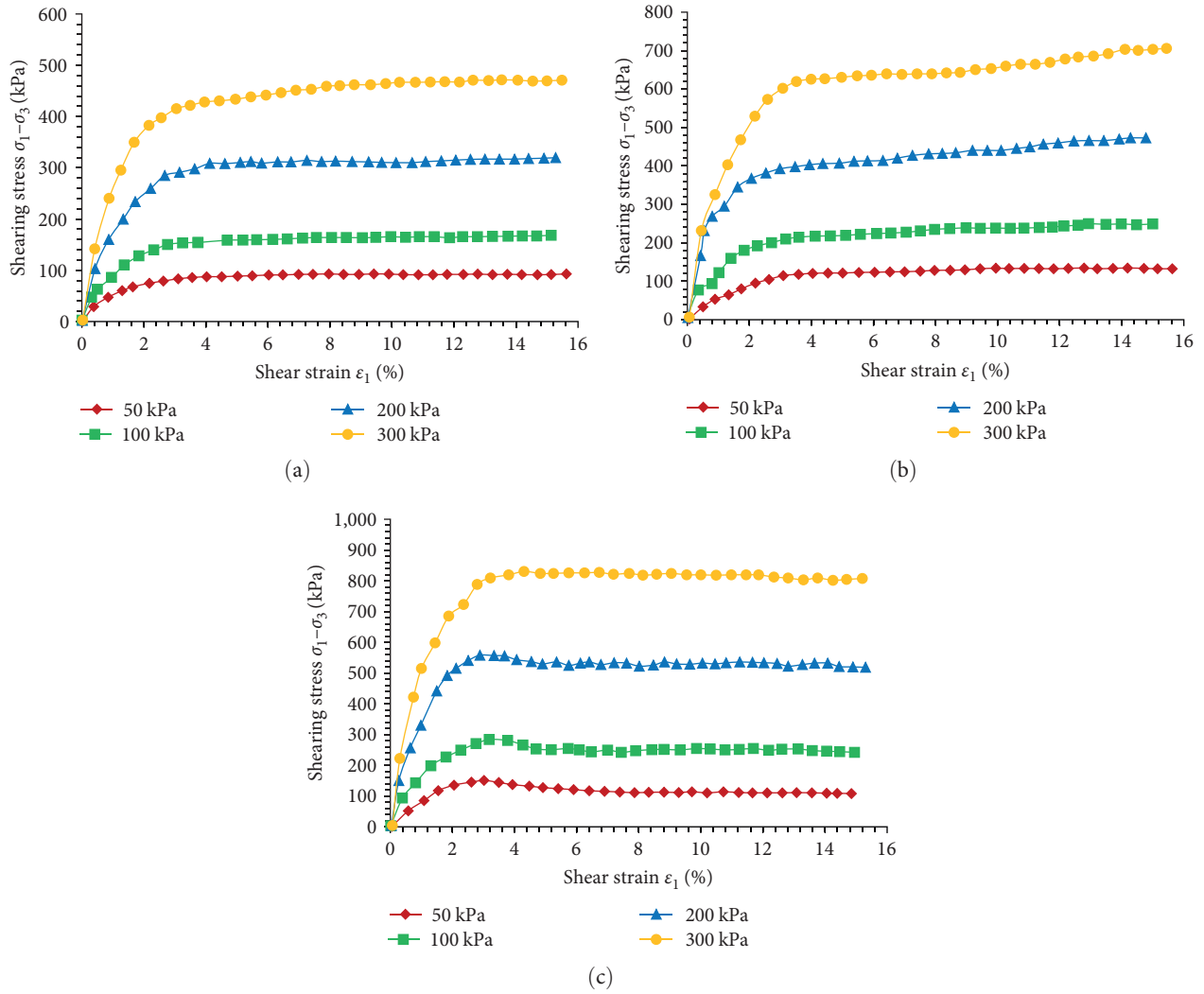
FIGURE 6: Stress–strain relationship curves for consolidated-drained tests on tailings samples: (a) sample 1[#]; (b) sample 2[#]; (c) sample 3[#].
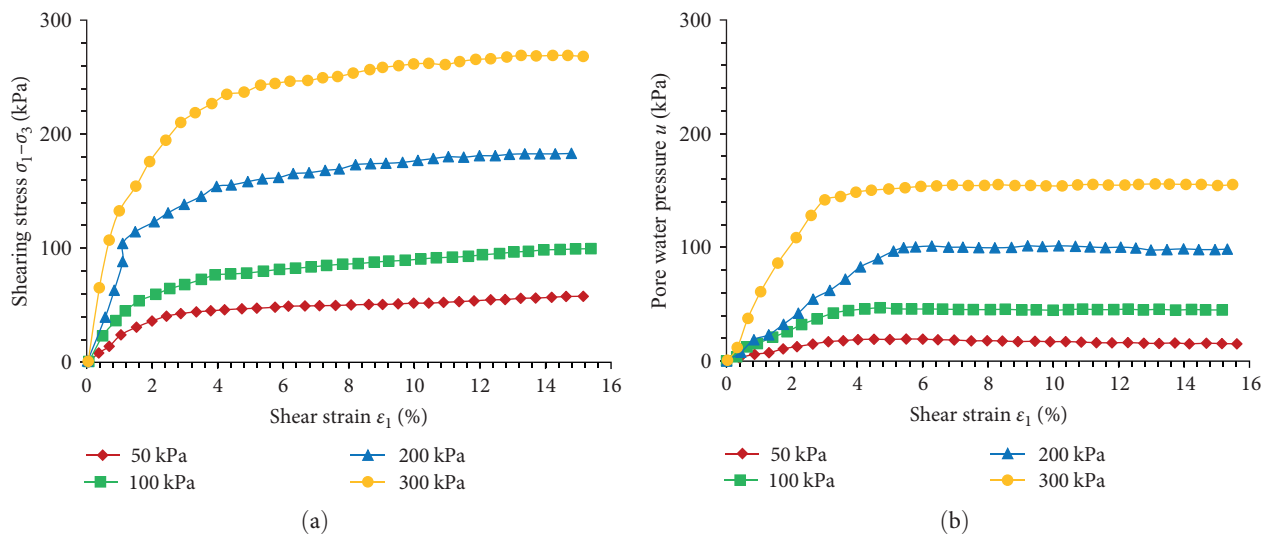

FIGURE 7: Stress–strain and pore water pressure–strain relationship curves for consolidation-undrained test on 1[#] tailings sample: (a) shearing stress; (b) pore water pressure.
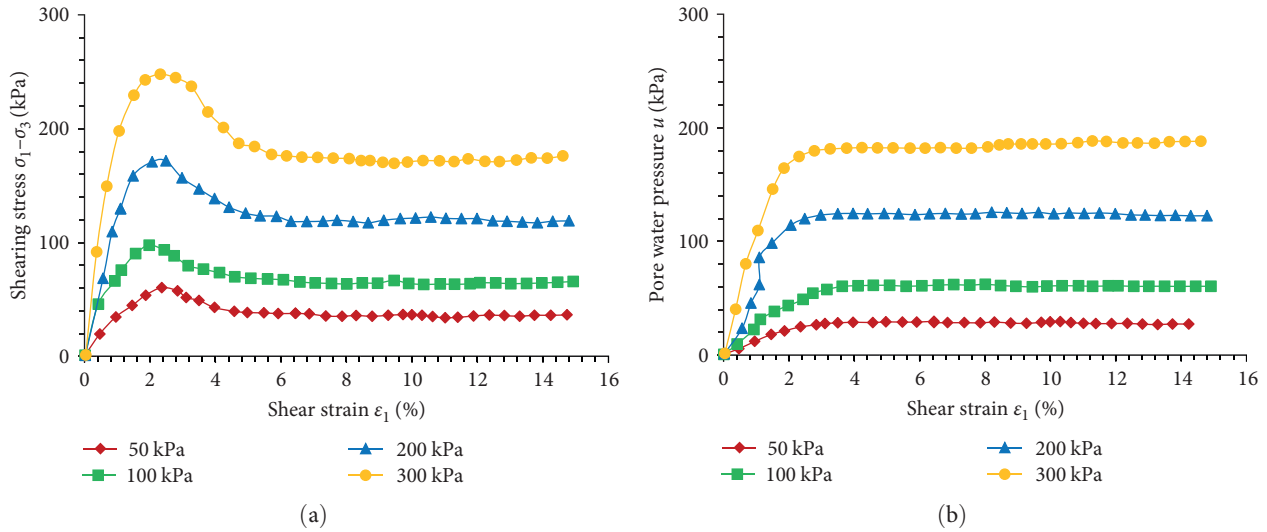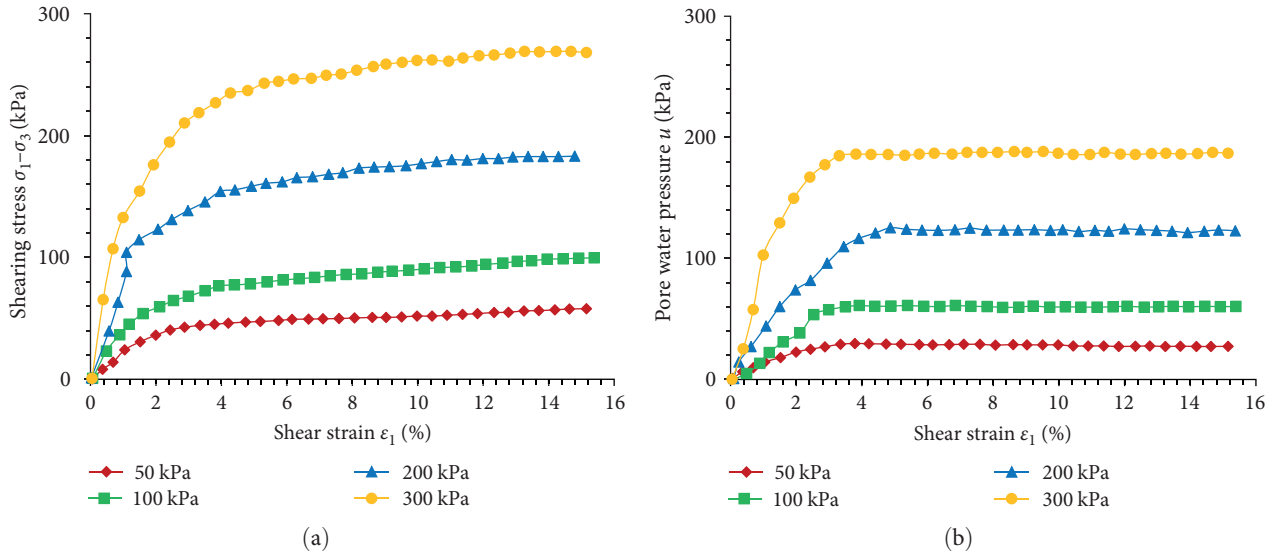
FIGURE 8: Stress–strain and pore water pressure–strain relationship curves for consolidation-undrained test on $2^{\#}$ tailings sample: (a) shearing stress; (b) pore water pressure.

FIGURE 9: Stress–strain and pore water pressure–strain relationship curves for consolidation-undrained test on $3^{\#}$ tailings sample: (a) shearing stress; (b) pore water pressure.

shown in Figure 7(a)) mirrors the curve under drained conditions (Figure 6(a)), displaying positive excess pore water pressure during shearing. Conversely, the curve for sample $2^{\#}$ (a silty sandy tailing, shown in Figure 8(a)) does not exhibit positive pore pressure during shearing, indicative of the deformation and strength of silty sandy tailings being more responsive to effective confining pressure. In contrast to silty clay tailing, sample $1^{\#}$ demonstrates a cohesive strength that is not significantly influenced by confining pressure.

For sample $2^{\#}$, the silty sandy tailing, under low confining pressure (50 kPa), the stress–strain relationship demonstrates strain-softening behavior, contrasting with that observed in drained tests (Figure 8). The peak stress, reaching 60 kPa, occurs at an axial strain of 2%. As strain increases, the effective confining pressure sharply decreases, and the stress difference

$\sigma_1 - \sigma_3$ rapidly reduces to 38 kPa at an axial strain of 5%. Subsequently, the stress difference stabilizes, with pore pressure remaining unchanged and the corresponding effective confining pressure $\sigma'3$ reducing to merely 12 kPa. This behavior is indicative of static liquefaction. The assessment of silty sandy tailings strength through consolidated-undrained tests is crucial. Under a confining pressure of 400 kPa, the peak stress difference $(\sigma_1-\sigma_3)_{\max}$ reaches 247 kPa for the silty sandy tailing, correlating to a consolidated-undrained friction angle φ_{cu} of 14.5°. At this stage, the stress state of the tailings has yet to attain its strength capacity, but the sample undergoes flow-like behavior. However, upon reaching a steady state, despite the deviator stress $(\sigma_1-\sigma_3)_{ult}$ being only 50 kPa, the effective stress friction angle φ' amounts to 30.5°, while the corresponding undrained friction angle is 15.8°. This marks the
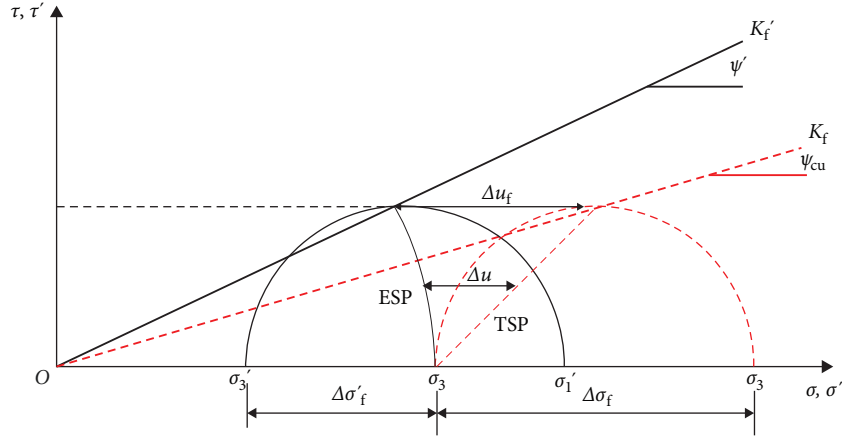
FIGURE 10: Stress path of triaxial consolidation-undrained test.

TABLE 3: Shear strength parameters.

Sample number	Type	Consolidation-undrained				Consolidation drained	
		Total stress shear strength index		Effective stress shear strength index			
		Cohesion φ (°)	Internal friction angle c (kPa)	Effective cohesion φ (°)	Effective internal friction angle c (kPa)	Cohesion φ (°)	Internal friction angle c (kPa)
1[#]	Silty clay tailing	14.5	5.9	25.1	1.2	27.5	5.3
2[#]	Silt tailing	15.8	8.6	30.5	5.4	32.2	5.9
3[#]	Sandy silt tailing	17.3	5.7	32.2	3.2	35.1	4.1

point where the silty sandy tailing sample achieves a state of failure.

The permeability coefficient of sample 3[#], classified as silty sandy tailing, exhibits a relatively high value. This implies that under very slow loading rates, there is sufficient time for internal water to drain. However, in scenarios involving earthquakes, landslides, or the presence of tailings mud layers within the tailings dam, the pore water pressure within the silty sandy tailing may reach excessive levels, as illustrated in Figure 9. Consequently, consolidated-undrained shear tests are essential under such conditions.

Figure 10 depicts the stress paths, namely the total stress and effective stress paths, along with their corresponding indicators for effective stress strength and total stress strength. The angle formed between the failure principal stress line K_f (K'_f) and the σ (σ') axis is denoted as ψ (ψ'), where $\tan(\psi_{cu}) = \sin(\varphi_{cu})$. The total stress path is referred to as TSP, while the effective stress path is known as ESP. It is noteworthy that during the loading of the silty clay tailing specimen, as the pore pressure is positive, the effective stress consistently appears to the left of the total stress path, implying that $\varphi' > \varphi_{cu}$.

3.2.3. Comparison of Test Results under Drained and Undrained Conditions.

Identifying the peak of the effective principal stress ratio as the failure point enabled the determination of both total stress and effective stress shear strength indicators for tailings sand and tailings sludge. The experimental results are presented in Table 3. Based on these results, the following conclusions were drawn:

(1) Under consolidated-drained conditions, the internal friction angle of silty clay tailing shows an increase, attributed to the gradual drainage of pore water, leading to an increased vertical effective stress. Consequently, the tailings demonstrate enhanced consolidation and a higher internal friction angle.

(2) Under consolidated-undrained conditions, the effective internal friction angles for tailings sand and tailings silt are similar, while the angle for silty clay tailing is markedly lower. This phenomenon occurs because, under such conditions, the vertical stress is primarily supported by pore water, reducing the vertical stresses between tailings particles and thus lowering the internal friction angle φ_{cu}.

(3) For normally consolidated silty clay tailing specimens, both drained and undrained shear tests show failure principal stress lines passing through the origin, indicating a cohesion value c of 0. Furthermore, $\varphi' > \varphi_{cu}$, with φ_{cu} being approximately half of φ'. The effective stress strength indicators derived from consolidated-undrained tests, c' and φ', are deemed consistent with the strength indicators cd and φ_d obtained from consolidated-drained tests. However, this is contingent upon the sample type and the defined failure criteria. In triaxial tests, failure strength is typically characterized as either the maximum shear stress $(\sigma_1 - \sigma_3)_{max}$ or the maximum stress ratio $(\sigma_1/\sigma_3)_{max}$. In the context of consolidated-undrained tests on tailings sand, applying these two distinct failure strength
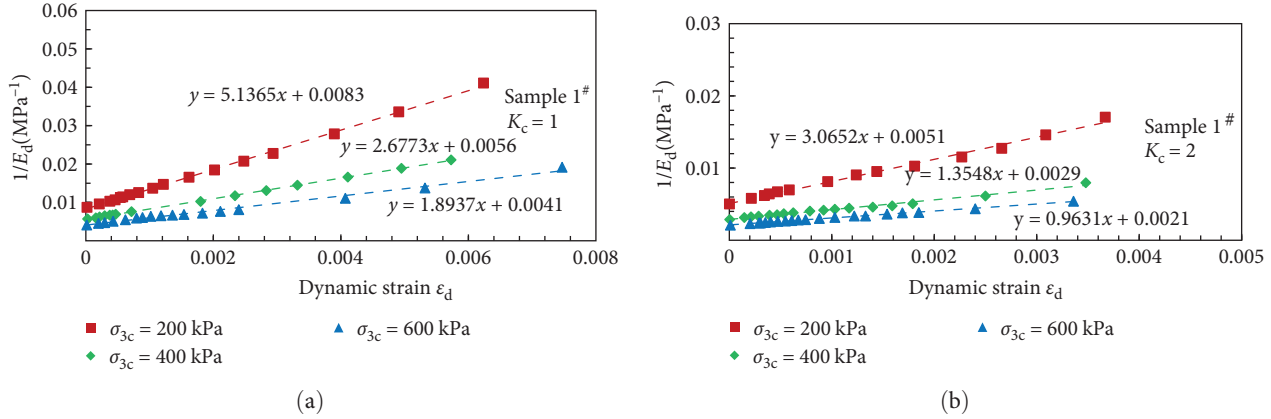
(a)

(b)

FIGURE 11: ($1/E_d \sim \varepsilon_d$) curves of sample 1[#]: (a) $K_c = 1$; (b) $K_c = 2$.
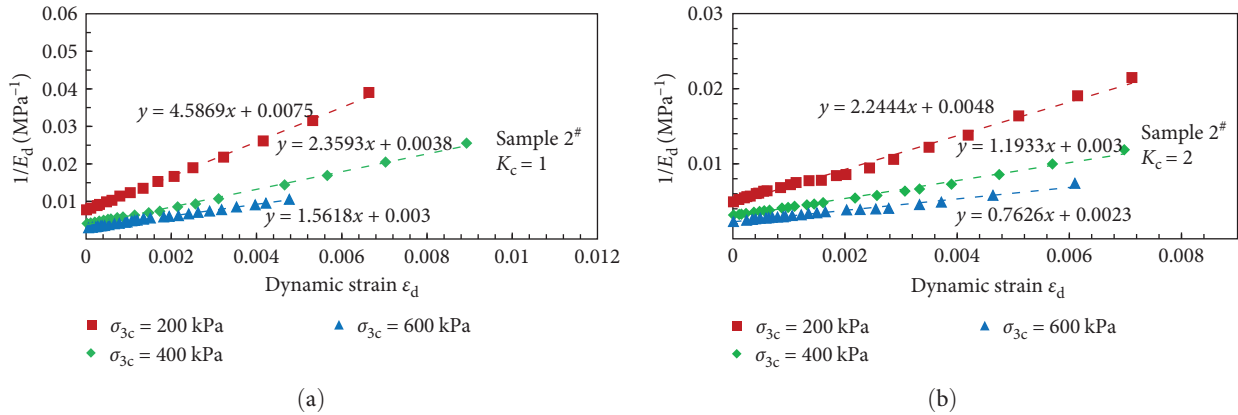

(a)

(b)

FIGURE 12: ($1/E_d \sim \varepsilon_d$) curves of sample 2[#]: (a) $K_c = 1$; (b) $K_c = 2$.

definitions can lead to significant differences in the internal friction angle.

4. Dynamic Characteristics of Tailings

Since the 1960s, particularly following events like the 1964 Niigata Earthquake in Japan and the 1964 Alaska Earthquake in the United States, increased awareness has emerged regarding the disasters caused by earthquakes. Although earthquake loads are irregular by nature, research often simplifies them into equivalent periodic loads. In this study, earthquake effects were simulated using a sinusoidal load with a frequency of 1 Hz. Due to the substantial presence of quartz, tailings particles exhibit weak hydrophilicity. Saturated and loose tailings display highly sensitive structural characteristics. Under cyclic loading conditions, tailings possess relatively low dynamic strength and a limited range of dynamic shear stress ratios, making them susceptible to liquefaction and failure. Consequently, the dynamic characteristics of tailings are integral to the safety and stability of tailings dams.

4.1. Dynamic Modulus. Figures 11–13 illustrate the typical inverse relationships between the dynamic elastic modulus,

denoted as $1/E_d$, and the axial dynamic strain, ε_d, for the three tailings materials. These variables can be effectively depicted as straight lines on a graph. The behavior of E_d and ε_d exhibits a hyperbolic trend; therefore, they can be accurately described using the Hardin viscoelastic model. The formula for this model is outlined below:

$$\sigma_d = \varepsilon_d / (1/E_0 + \varepsilon_d / \sigma_{dmax}), \tag{1}$$

where E_0 is the initial dynamic elastic modulus, σ_{dmax} is the maximum dynamic stress, E_0 and σ_{dmax} are the intercepts and the reciprocal of the slope of the $1/E_d \sim \varepsilon_d$ relationship straight line, respectively.

In the analysis of dynamic response using an equivalent viscoelastic model, the following relationships exist between dynamic shear strain γ_d and dynamic axial strain ε_d, dynamic shear modulus G_d and dynamic compression modulus E_d, and maximum dynamic shear stress τ_{dmax} and maximum dynamic stress σ_{dmax}:

$$G_d = \frac{E_d}{[2(1+\mu)]}, \tag{2}$$

$$\gamma_d = \varepsilon_d (1 + \mu), \tag{3}$$
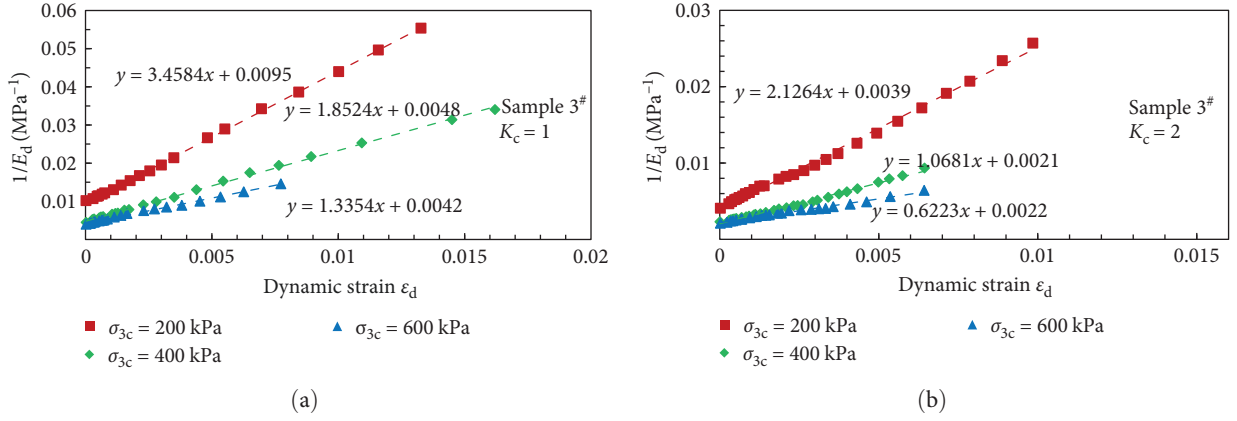
FIGURE 13: $(1/E_d \sim \varepsilon_d)$ curves of sample $3^{\#}$: (a) $K_c = 1$; (b) $K_c = 2$.
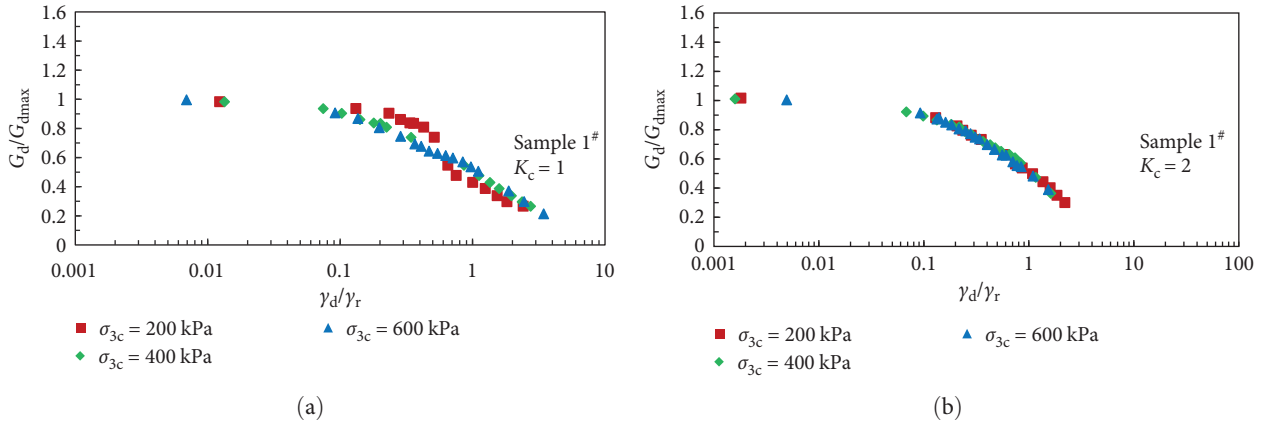
FIGURE 14: $G_d/G_{dmax} \sim \gamma_d/\gamma_r$ curves of sample $1^{\#}$: (a) $K_c = 1$; (b) $K_c = 2$.

$$\tau_{dmax} = \frac{\sigma_{dmax}}{2}, \qquad (4)$$

where μ is the Poisson's ratio.

For saturated undrained conditions, no volume change is noted ($\varepsilon_v = 0$). Under axisymmetric triaxial stress conditions, $\varepsilon_v = \varepsilon_1 + 2\varepsilon_3$. Therefore, μ can be taken as 0.5.

Based on Equations (2)–(4), Equation (1) can be transformed into the following:

$$G_d/G_{dmax} = 1/(1 + \gamma_d/\gamma_r), \qquad (5)$$

where G_{dmax} is the initial shear modulus, and $\gamma_r = G_{dmax}/\tau_{dmax}$ is the reference strain.

According to Equation (5), the dynamic shear modulus G_d of tailings at any dynamic strain can be determined. However, the two parameters G_{dmax} and τ_{dmax} in the equation should be determined through dynamic shear tests under different consolidation stress conditions for the three types of tailings. Figures 14–16 show the variations of G_d/G_{dmax} with γ_d/γ_r under different consolidation ratios K_c conditions.

4.2. Damping Ratios.
In the relationships observed between damping ratio λ and dynamic shear strain γ_d, as depicted in Figures 17–19, certain characteristics emerge.

When examining under a constant consolidation stress ratio K_c across various effective consolidation stress σ'_{3c} conditions, the relationship between damping ratio λ and dynamic shear strain γ_d remains within a narrow band. This pattern holds true under varying consolidation stress ratio K_c conditions at a fixed effective consolidation stress σ'_{3c}, indicating that changes in effective consolidation stress σ'_{3c} and consolidation stress ratio K_c exert minimal influence on the damping ratio of tailings.

As dynamic shear strain γ_d increases, a corresponding rise in damping ratio λ is observed. Notably, the relationship between damping ratio λ and dynamic shear strain γ_d can be segmented into three distinct phases: a gentle increase, a rapid growth phase, and a plateau stage. For smaller strain values ($\gamma_d < 10^{-3}$), tailings demonstrate a relatively low damping ratio. However, as strain escalates ($\gamma_d > 10^{-3}$), the damping ratio rapidly ascends before reaching a state of stability.

Drawing from experimental data in this study, the damping ratio λ stabilizes when dynamic shear strain γ_d approximates 0.01. Thus, the damping ratio value λ at $\gamma_d = 0.01$ is designated as λ_{max}, serving as the reference for tailings' damping ratio under these specific conditions.
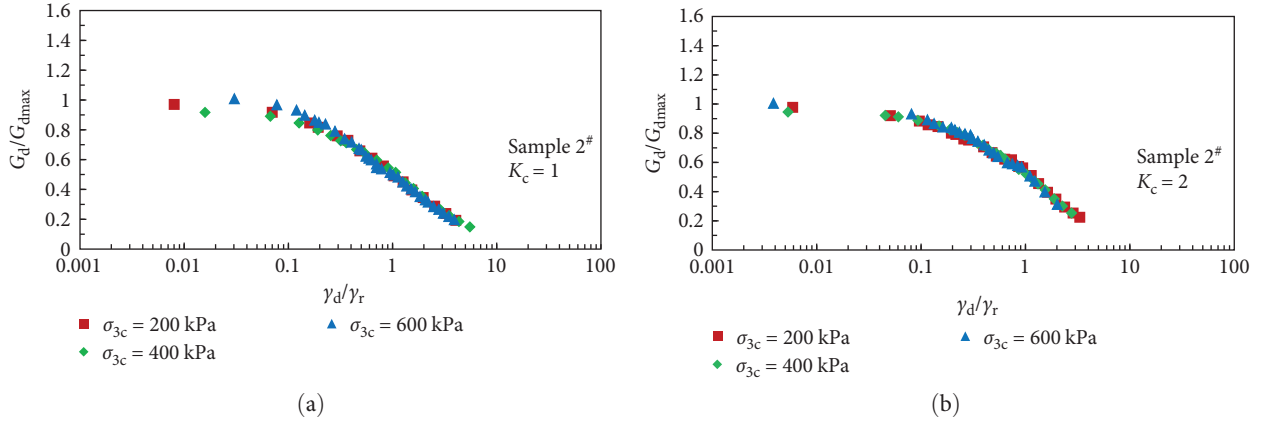
(a)

(b)

FIGURE 15: $G_d/G_{dmax} \sim \gamma_d/\gamma_r$ curves of sample 2$^\#$: (a) $K_c = 1$; (b) $K_c = 2$.
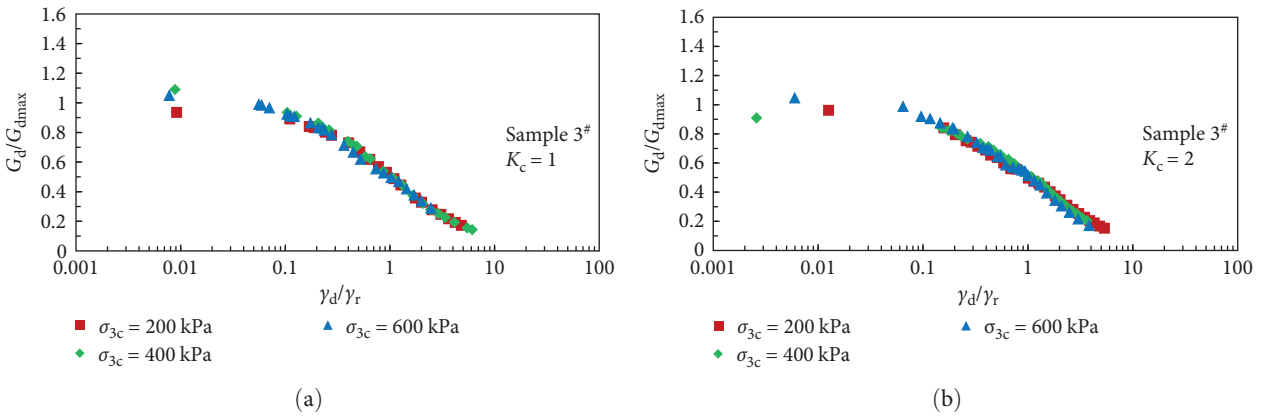

(a)

(b)

FIGURE 16: $G_d/G_{dmax} \sim \gamma_d/\gamma_r$ curves of sample 3$^\#$: (a) $K_c = 1$; (b) $K_c = 2$.
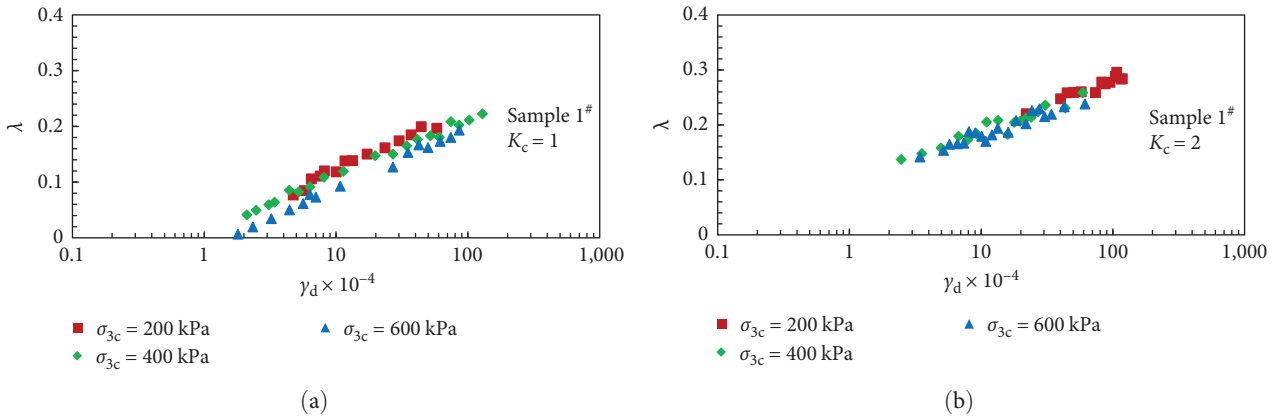

(a)

(b)

FIGURE 17: $\lambda \sim \gamma_d$ curves of sample 1$^\#$: (a) $K_c = 1$; (b) $K_c = 2$.

In a double logarithmic coordinate system, the typical relationship between (λ/λ_{max}) and $(1 - G_d/G_{dmax})$ under different consolidation stress conditions (as shown in Figures 20–22) can be approximately normalized to a straight line, which can be expressed as follows:

$$\lambda/\lambda_{max} = (1 - G_d/G_{dmax})^m, \qquad (6)$$

where m is the experimental parameter, which slightly varies for different tailings samples but remains relatively constant. The average value is 0.538.

4.3. Dynamic Strength. Dynamic strength tests are conducted by applying dynamic stress to consolidated samples and subjecting them to vibrations until failure is observed. Throughout the
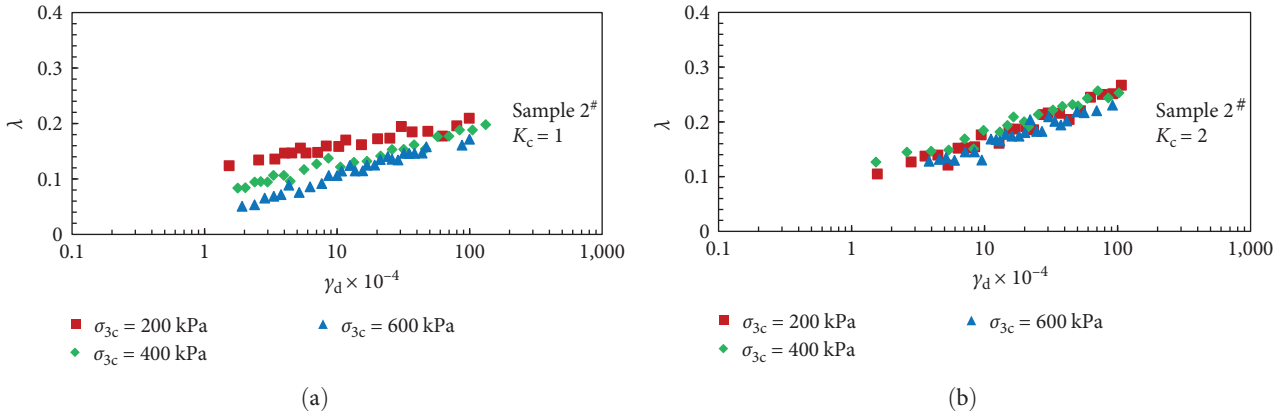
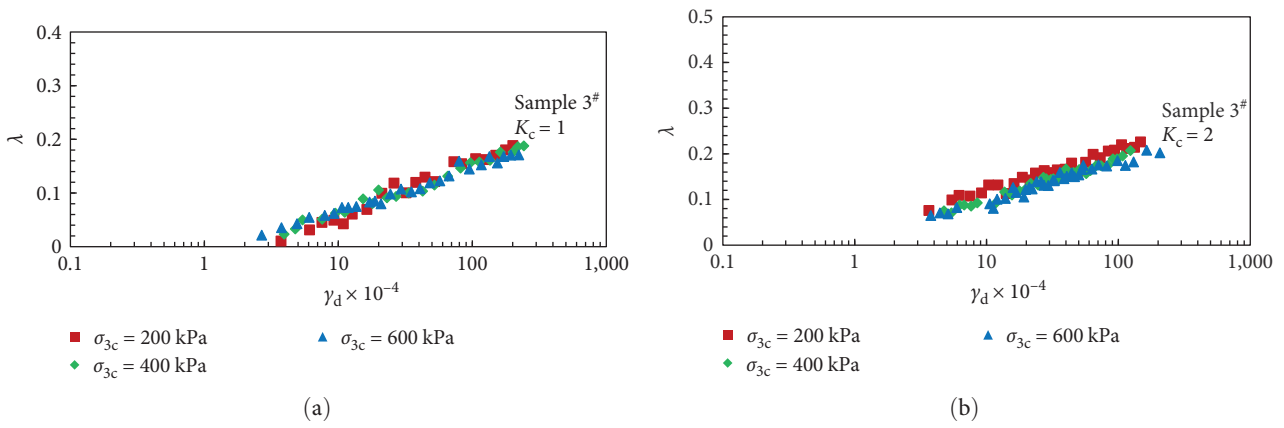FIGURE 18: $\lambda \sim \gamma_d$ curves of sample $2^{\#}$: (a) $K_c = 1$; (b) $K_c = 2$.

FIGURE 19: $\lambda \sim \gamma_d$ curves of sample $3^{\#}$: (a) $K_c = 1$; (b) $K_c = 2$.
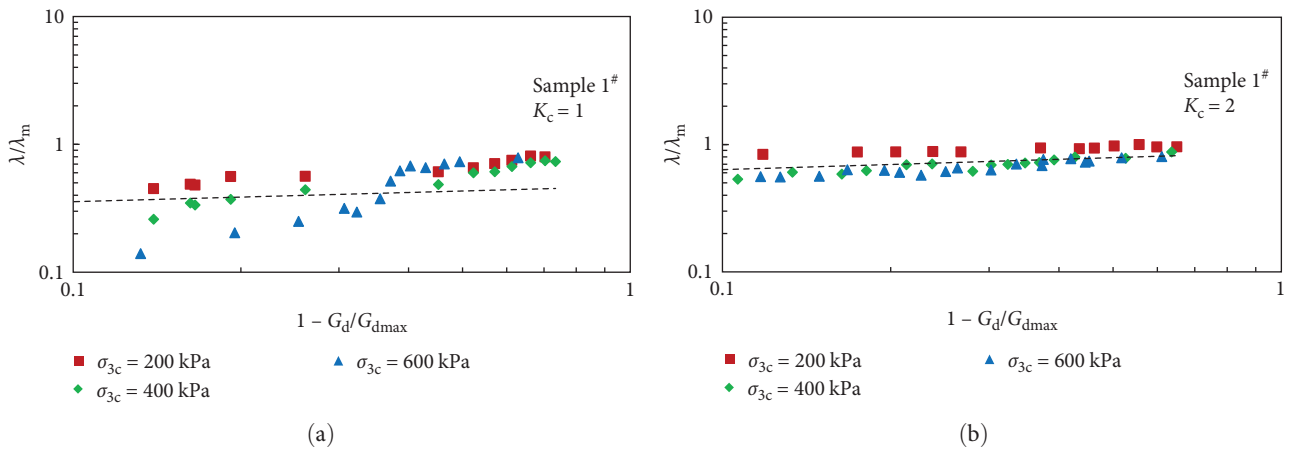

FIGURE 20: $\lambda/\lambda_m \sim 1 - G_d/G_{dmax}$ curves of sample $1^{\#}$: (a) $K_c = 1$; (b) $K_c = 2$.

test, variations in dynamic stress, strain, and pore pressure are monitored using a computer system. Under consistent test conditions, including the consolidation stress ratio and confining pressure, multiple dynamic stress levels are applied for dynamic strength assessment. For isotropic consolidation conditions, the criterion for failure is when the pore pressure matches the confining pressure. In contrast, for anisotropic consolidation, different strain criteria are established, setting residual strain at 5% or a combined strain (sum of elastic and residual strains) at 10% as the failure threshold. The failure cycles, denoted as N_f, representing the vibration cycles needed to induce failure under specific dynamic stresses, are determined based on these criteria.
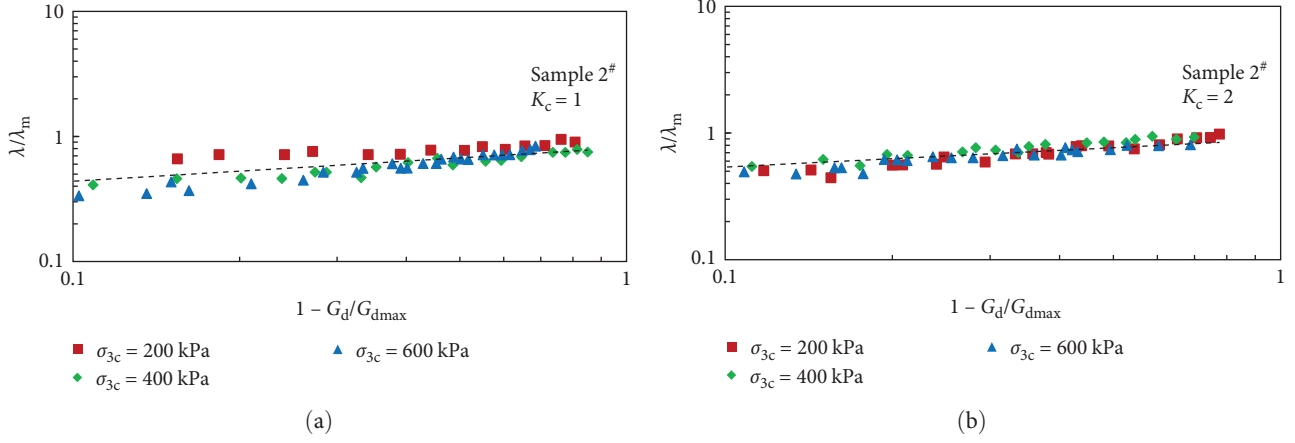
FIGURE 21: $\lambda/\lambda_{\mathrm{m}} \sim 1-G_{\mathrm{d}}/G_{\mathrm{dmax}}$ curves of sample 2$^{\#}$: (a) $K_{\mathrm{c}} = 1$; (b) $K_{\mathrm{c}} = 2$.
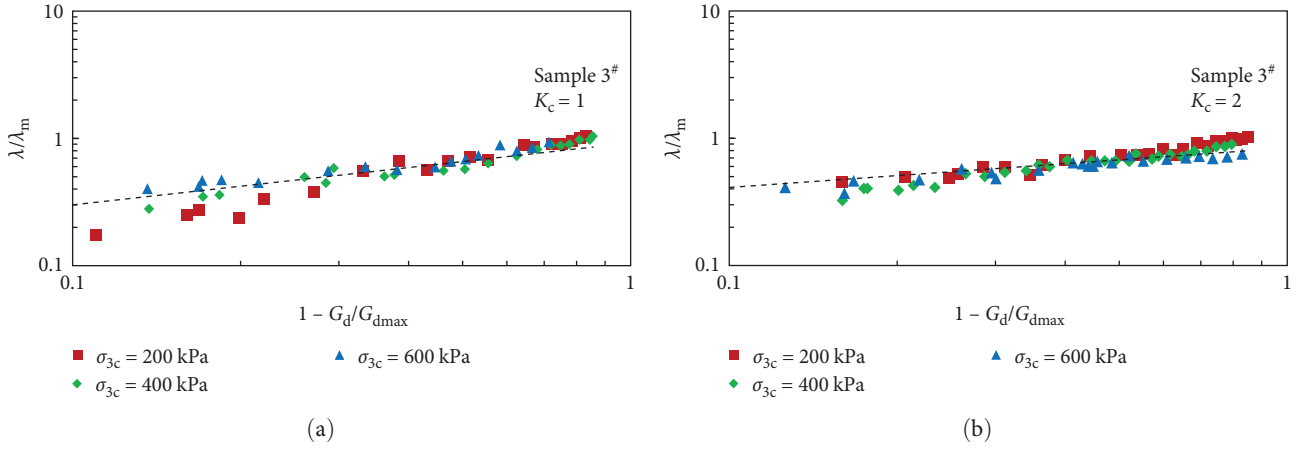
FIGURE 22: $\lambda/\lambda_{\mathrm{m}} \sim 1-G_{\mathrm{d}}/G_{\mathrm{dmax}}$ curves of sample 3$^{\#}$: (a) $K_{\mathrm{c}} = 1$; (b) $K_{\mathrm{c}} = 2$.

The relationship between $\sigma_{\mathrm{d}}/2\sigma_{3\mathrm{c}}$ and N_{f} under different dynamic stresses is plotted, resulting in the curves depicted in Figures 23–25.

Based on the dynamic modulus test and dynamic strength test results from the dynamic triaxial tests, the parameters of the Zhujiang–Shen computational model are determined. Using Equations (7) and (8), the values of σ_{e} (equivalent stress), and the corrected dynamic strain amplitude γ_{c} are calculated.

$$\sigma_{\mathrm{e}} = 1/2(\sigma_{1\mathrm{c}}/\sigma_{3\mathrm{c}}) - u_{\mathrm{d}} + c.ctg\varphi, \tag{7}$$

$$\gamma_{\mathrm{c}} = (\gamma_{\mathrm{c}})^{3/4}/(\sigma_{\mathrm{e}})^{1/2}, \tag{8}$$

where u_{d} represents the average pore pressure for each cycle, c and φ are the static shear strength parameters of the tailings sample (using the values from Table 3), and γ_{d} is the dynamic shear strain amplitude.

Plotting the calculated results on graphs with the vertical axis as $(\sigma_{\mathrm{e}})1/2/G_{\mathrm{d}}$ and the horizontal axis as γ_{c}, as shown in Figures 26–28. Drawing a straight line with an intercept of

$1/K_2$ and a slope of K_1/K_2 enables us to determine the values of K_1 and K_2.

For isotropic consolidation samples ($K_{\mathrm{c}} = 1$), the failure criterion is established when the vibration-induced pore pressure equals the consolidation pressure. In contrast, for anisotropic consolidation ($K_{\mathrm{c}} = 2$), the failure criterion is an axial residual strain of 5%. Referring to the σ_{d} vs. N_{f} relationship curve in Figure 26 and identifying the corresponding N_{f} value of 10 allows for determining the dynamic failure stress σ_{d} for 10 cycles of vibration at a specific $\sigma_{3\mathrm{c}}$. Subsequently, the dynamic shear stress ratio $(\tau_{\mathrm{d}}/\sigma_{3\mathrm{c}})_{10}$ for 10 vibration cycles is calculated, enabling the establishment of R_0 and R_1 values for both isotropic and anisotropic consolidation conditions. The values of R_0, R_1, and H_1 under varying conditions are determined and presented in Tables 4 and 5.

5. Conclusions

In this study, we conducted a series of compression, shear, and dynamic tests to investigate the pore ratio, compressibility modulus, shear stress–strain relationship, dynamic modulus, damping ratios, and dynamic strength of tailings from
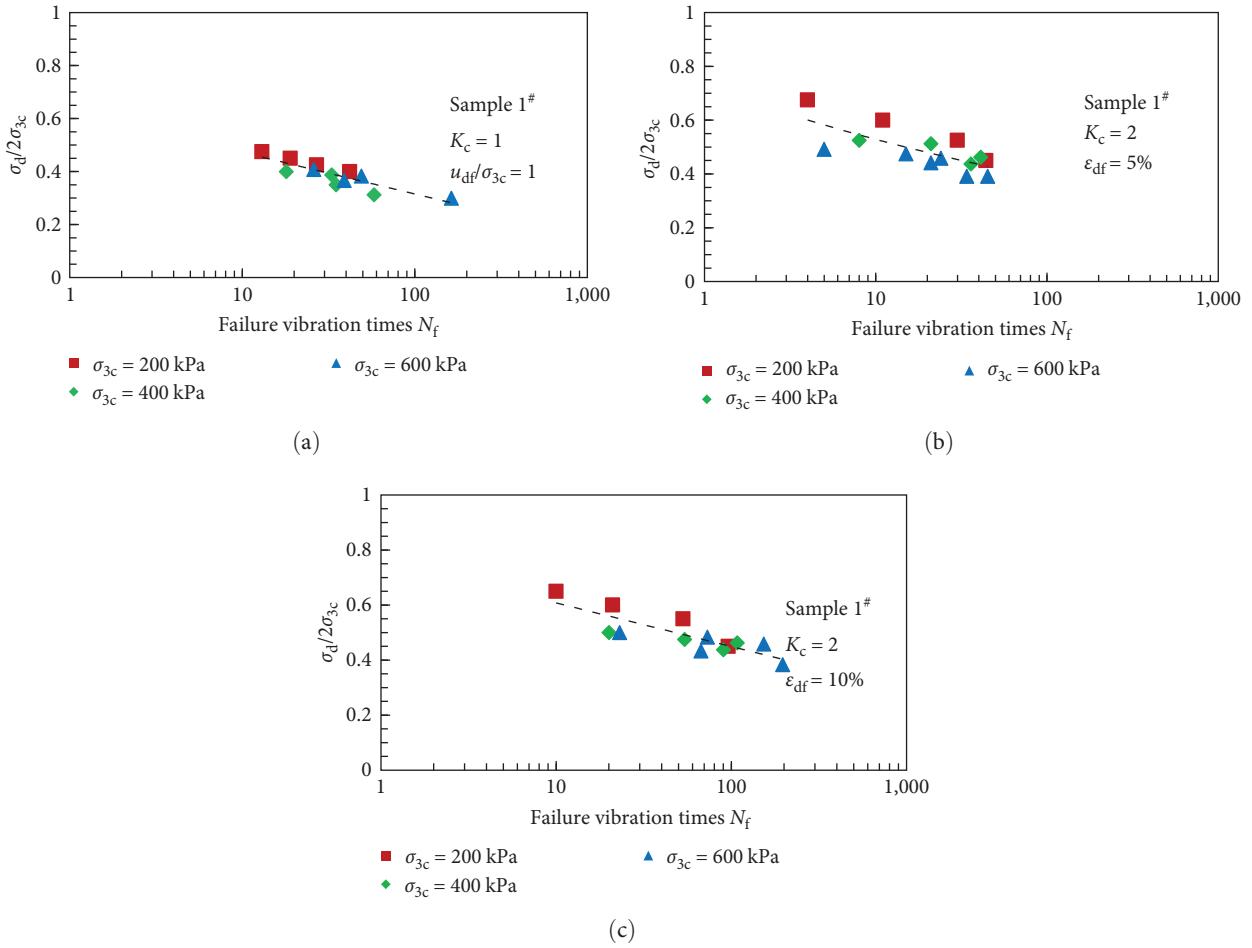
FIGURE 23: $\sigma_d \sim N_f$ curves of sample $1^{\#}$: (a) $K_c = 1$, $u_{df}/\sigma_{3c} = 1$; (b) $K_c = 2$, $\varepsilon_{df} = 5\%$; (c) $K_c = 2$, $\varepsilon_{df} = 10\%$.
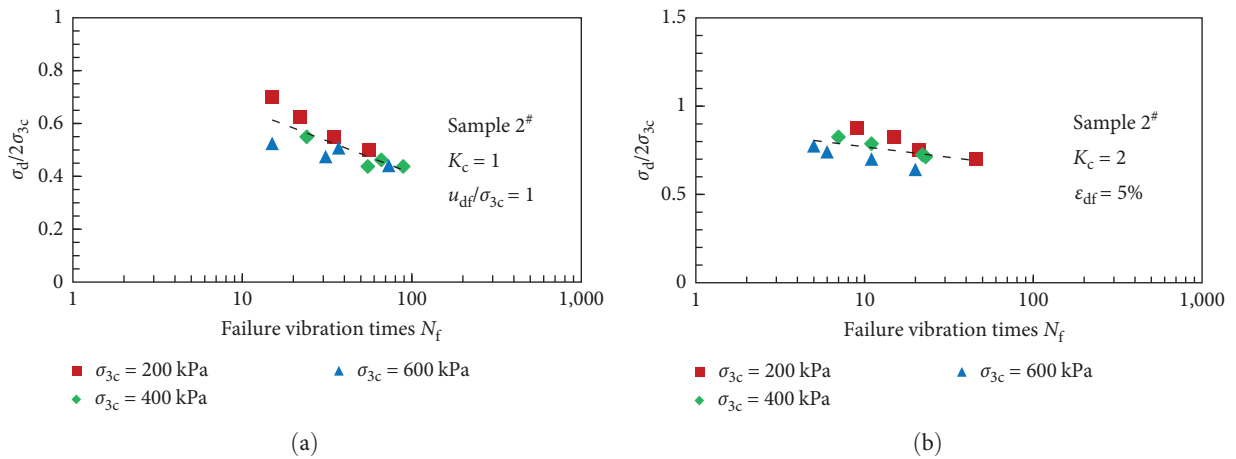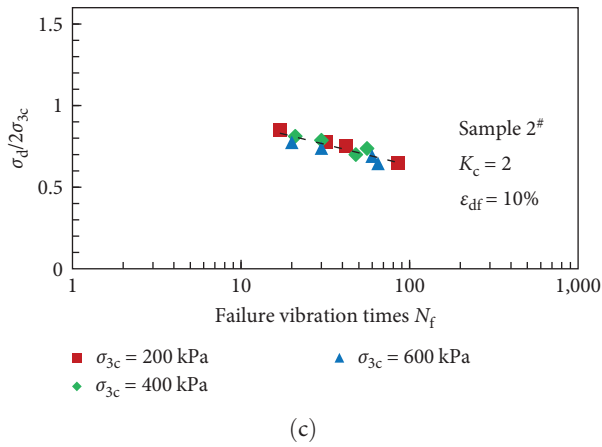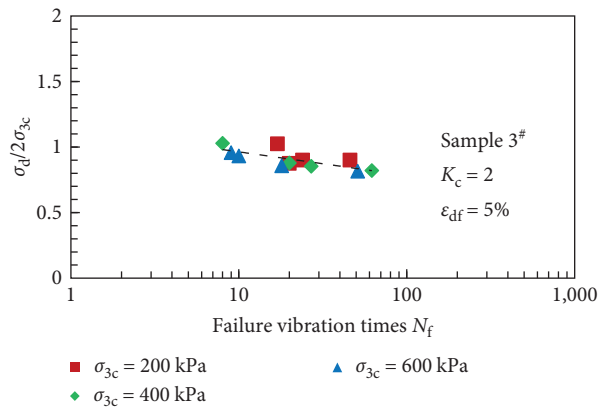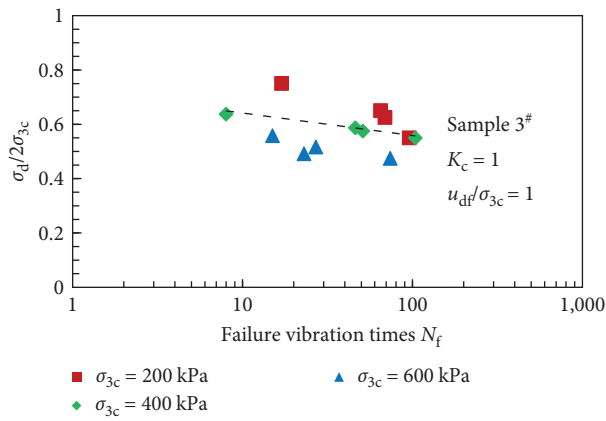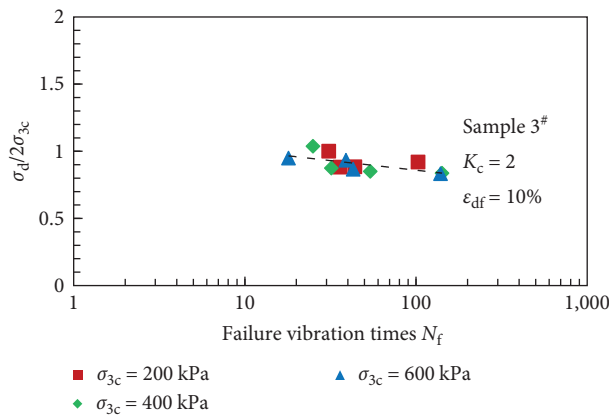

FIGURE 24: Continued.

(c)

FIGURE 24: $\sigma_d \sim N_f$ curves of sample $2^\#$: (a) $K_c = 1$, $u_{df}/\sigma_{3c} = 1$; (b) $K_c = 2$, $\varepsilon_{df} = 5\%$; (c) $K_c = 2$, $\varepsilon_{df} = 10\%$.
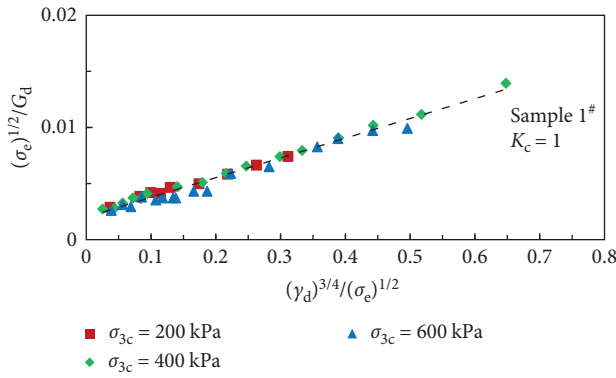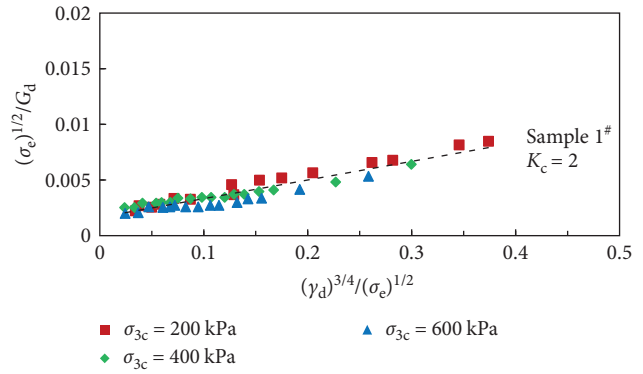

(a)

(b)

(c)

FIGURE 25: $\sigma_d \sim N_f$ curves of sample $3^\#$: (a) $K_c = 1$, $u_{df}/\sigma_{3c} = 1$; (b) $K_c = 2$, $\varepsilon_{df} = 5\%$; (c) $K_c = 2$, $\varepsilon_{df} = 10\%$.

FIGURE 26: $(\sigma_e)^{1/2}/G_d \sim \gamma_c$ curves of sample $1^\#$: (a) $K_c = 1$; (b) $K_c = 2$.

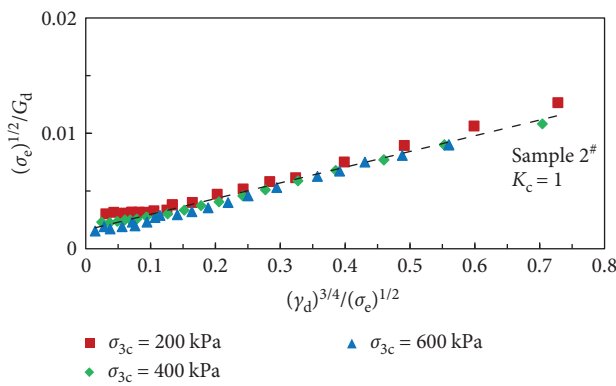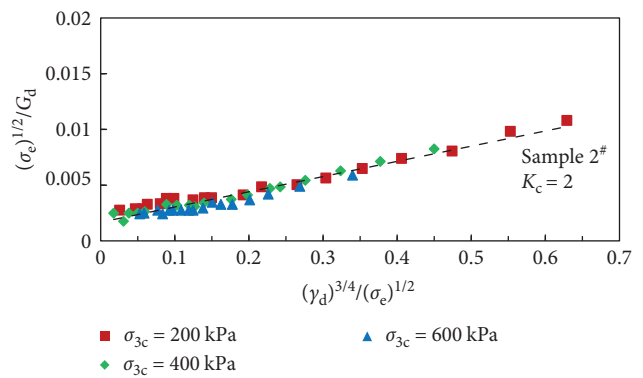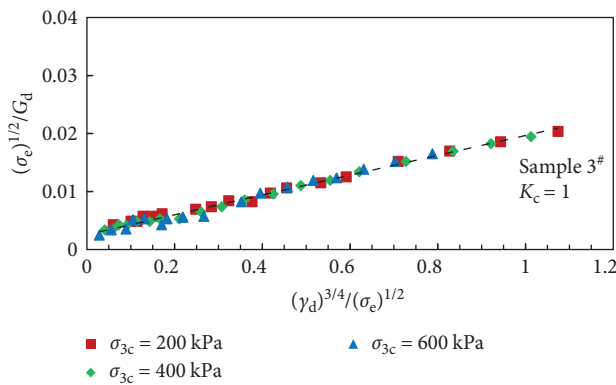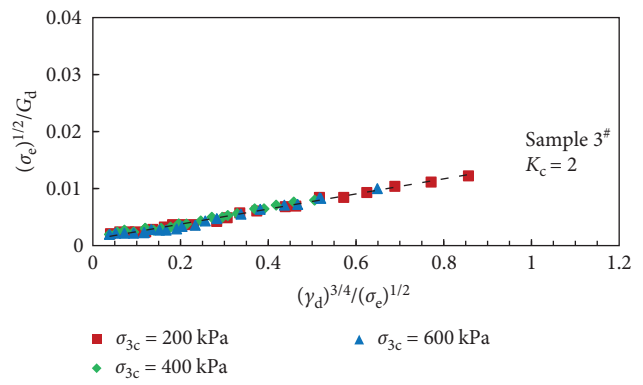FIGURE 27: $(\sigma_e)^{1/2}/G_d \sim \gamma_c$ curves of sample $2^\#$: (a) $K_c = 1$; (b) $K_c = 2$.

FIGURE 28: $(\sigma_e)^{1/2}/G_d \sim \gamma_c$ curves of sample $3^\#$: (a) $K_c = 1$; (b) $K_c = 2$.

TABLE 4: Parameters of Zhujiang–Shen calculation model ($K_c = 1$).

Sample number	σ_{3c} (kPa)	K_1	K_2	R_0
$1^{\#}$	200			0.491
	400	8.80	500	0.452
	600			0.459
$2^{\#}$	200			0.752
	400	8.33	417	0.618
	600			0.547
$3^{\#}$	200			0.813
	400	8.52	625	0.632
	600			0.557

TABLE 5: Parameters of Zhujiang–Shen calculation model ($K_c = 2$).

Sample number	σ_{3c} (kPa)	K_1	K_2	R_1	H_1
$1^{\#}$	200			0.601	0.296
	400	9.82	588	0.523	0.154
	600			0.474	0.094
$2^{\#}$	200			0.858	0.414
	400	8.15	545	0.794	0.174
	600			0.705	0.078
$3^{\#}$	200			0.991	0.454
	400	12.65	909	0.967	0.223
	600			0.933	0.182

different depositional areas. The results led to the following conclusions:

(i) Proximity to the initial dam influences tailings particle size and void ratio; the closer the tailings, the coarser the particles and the smaller the initial void ratio, leading to reduced compressibility.

(ii) Compression tests on naturally deposited tailings reveal that finer particles are associated with looser tailings and greater compressibility. An increase in vertical pressure causes a decrease in void ratio, with the e-lgp curve resembling two linear segments.

(iii) A comparison of consolidated-drained and consolidated-undrained tests across the three tailings samples shows that finer particles significantly affect the divergence in effective stress strength indicators between these two conditions.

(iv) The stress–strain relationship of the three tailings types aligns with the Hardin equivalent viscoelastic model. With increasing shear strain, the damping ratio progresses through three distinct phases: initial gradual increase, rapid growth, and subsequent gradual stabilization. Furthermore, dynamic shear strength at failure escalates with higher effective consolidation confining pressure and increased consolidation stress ratio.

Data Availability

The data presented in this study are available on request from the corresponding author.

Conflicts of Interest

The authors declare that there are no conflicts of interest.

Authors' Contributions

Conceptualization has done by Longfei Zhang and Zaiqiang Hu; methodology has done by Longfei Zhang and Hongru Li; validation has done by Longfei Zhang, Haicheng She, and Xiaoliang Wang; formal analysis has done by Haicheng She; investigation has done by Qiuxiang Qin and Xiaoliang Wang; writing—original draft has done by Longfei Zhang; writing—review and editing has done by Zaiqiang Hu; supervision has done by Haicheng She and Qiuxiang Qin. All authors have read and agreed to the published version of the manuscript.

Acknowledgments

References

[1] J. Stowe, I. Farrell, and E. Wingeard, "Tailings transport system design using probabilistic methods," *Mining, Metallurgy & Exploration*, vol. 38, no. 3, pp. 1289–1296, 2021.

[2] Q. Chen, H. Zhou, Y. Wang, D. Wang, Q. Zhang, and Y. Liu, "Erosion wear at the bend of pipe during tailings slurry transportation: numerical study considering inlet velocity, particle size and bend angle," *International Journal of Minerals, Metallurgy and Materials*, vol. 30, no. 8, pp. 1608–1620, 2023.

[3] A. J. Whittle, H. M. El-Naggar, S. A. Y. Akl, and A. M. Galaa, "Stability analysis of upstream tailings dam using numerical limit analyses," *Journal of Geotechnical and Geoenvironmental Engineering*, vol. 148, no. 6, pp. 1–14, 2022.

[4] M. Naeini and A. Akhtarpour, "Numerical analysis of seismic stability of a high centerline tailings dam," *Soil Dynamics and Earthquake Engineering*, vol. 107, pp. 179–194, 2018.

[5] J. Jin, H. Zhang, L. Xu, K. Zhou, and X. Lv, "Stability analysis of downstream dam expansion tailings pond," *Advances in Civil Engineering*, vol. 2022, Article ID 1809736, 13 pages, 2022.

[6] T. D. Stark, L. Moya, and J. Lin, "Rates and causes of tailings dam failures," *Advances in Civil Engineering*, vol. 2022, Article ID 7895880, 21 pages, 2022.

[7] L. Tang, X. Liu, X. Wang, S. Liu, and H. Deng, "Statistical analysis of tailings ponds in China," *Journal of Geochemical Exploration*, vol. 216, Article ID 106579, 2020.

[8] L. Piciullo, E. B. Storrøsten, Z. Liu, F. Nadim, and S. Lacasse, "A new look at the statistics of tailings dam failures," *Engineering Geology*, vol. 303, Article ID 106657, 2022.

[9] B. Shi, X. Li, W. Hu et al., "Environmental risk of tailings pond leachate pollution: traceable strategy for leakage channel and influence range of leachate," *Journal of Environmental Management*, vol. 331, Article ID 117341, 2023.

[10] V. Giuliano, F. Pagnanelli, L. Bornoroni, L. Toro, and C. Abbruzzese, "Toxic elements at a disused mine district: particle size distribution and total concentration in stream sediments and mine tailings," *Journal of Hazardous Materials*, vol. 148, no. 1-2, pp. 409–418, 2007.

[11] Z. Duan, H. Shi, Q. Li, Q. Liu, and Y. Yu, "Experimental characterization of the influence of ore drawing parameters on tailing deposition," *Geofluids*, vol. 2022, Article ID 7963836, 12 pages, 2022.

[12] C. Yao, L. Wu, J. Yang et al., "Influences of tailings particle size on overtopping tailings dam failures," *Mine Water and the Environment*, vol. 40, no. 1, pp. 174–188, 2021.

[13] G. Cao, W. Wang, G. Yin, and Z. Wei, "Experimental study of shear wave velocity in unsaturated tailings soil with variant grain size distribution," *Construction and Building Materials*, vol. 228, Article ID 116744, 2019.

[14] D. Adiguzel and A. Bascetin, "The investigation of effect of particle size distribution on flow behavior of paste tailings," *Journal of Environmental Management*, vol. 243, pp. 393–401, 2019.

[15] S. Tian, Y. He, R. Bai, J. Chen, and G. Wang, "Experimental study on consolidation and strength properties of tailings with different particle size distribution characteristics," *Natural Hazards*, vol. 114, no. 3, pp. 3683–3699, 2022.

[16] X. Song, Y. Hao, J. Huang, S. Wang, and W. Liu, "Study on mechanical properties and destabilization mechanism of unclassified tailings consolidation body under the action of dry-wet cycle," *Construction and Building Materials*, vol. 365, Article ID 130022, 2023.

[17] X. Huang, X. Cai, P. Yang, X. Zheng, S. Zhang, and J. Bo, "Study on the dynamic pore water pressure model of centerline tailings sand based on dynamic triaxial tests," *Geomechanics and Geophysics for Geo-Energy and Geo-Resources*, vol. 9, no. 1, pp. 1–12, 2023.

[18] X. Huang, X. Cai, J. Bo, S. Li, and W. Qi, "Experimental study of the influence of gradation on the dynamic properties of centerline tailings sand," *Soil Dynamics and Earthquake Engineering*, vol. 151, Article ID 106993, 2021.

[19] J.-X. Jin, H.-Z. Cui, L. Liang, S.-W. Li, and P.-Y. Zhang, "Variation of pore water pressure in tailing sand under dynamic loading," *Shock and Vibration*, vol. 2018, Article ID 1921057, 13 pages, 2018.

[20] H.-M. Liu, C.-H. Yang, C. Zhang, and H.-J. Mao, "Study on static and dynamic strength characteristics of tailings silty sand and its engineering application," *Safety Science*, vol. 50, no. 4, pp. 828–834, 2012.

[21] Y. Shan, J. Cui, H. Wen, S. Yu, and Y. Li, "Analysis of dynamic properties and transitional failure of clay–sand mixture in fine-grained soil based on mineral composition," *Engineering Geology*, vol. 296, Article ID 106464, 2022.

[22] M. James, M. Aubertin, D. Wijewickreme, and G. W. Wilson, "A laboratory investigation of the dynamic properties of tailings," *Canadian Geotechnical Journal*, vol. 48, no. 11, pp. 1587–1600, 2011.

[23] G. Sarkar and A. Sadrekarimi, "Undrained shearing behaviour of oil sands tailings," *Soil Dynamics and Earthquake Engineering*, vol. 161, Article ID 107410, 2022.

[24] X. Meng, S. A. Khoso, J. Kang et al., "A novel scheme for flotation tailings pulp settlement and chemical oxygen demand reduction with polyferric sulfate," *Journal of Cleaner Production*, vol. 241, Article ID 118371, 2019.

[25] R. B. Gomes, G. De Tomi, and P. S. Assis, "Iron ore tailings dry stacking in Pau Branco mine, Brazil," *Journal of Materials Research and Technology*, vol. 5, no. 4, pp. 339–344, 2016.

[26] C. Xuan, L. Shuang, Z. Han-Min, and C. Hui, "Reinforcement mechanism and engineering application of weak tailing pond beach by soilbag method," *Geofluids*, vol. 2022, Article ID 4015303, 8 pages, 2022.

[27] A. B. Fourie, G. E. Blight, and G. Papageorgiou, "Static liquefaction as a possible explanation for the Merriespruit tailings dam failure," *Canadian Geotechnical Journal*, vol. 38, no. 4, pp. 707–719, 2001.

[28] Y. Liu, E. Liu, X. Li, Y. Chen, H. Zhang, and H. Li, "Binary-medium constitutive model for freeze–thaw tailings subjected to cyclic triaxial loading," *Cold Regions Science and Technology*, vol. 213, Article ID 103927, 2023.

[29] S. Salam, M. Xiao, A. Khosravifar, and K. Ziotopoulou, "Seismic stability of coal tailings dams with spatially variable and liquefiable coal tailings using pore pressure plasticity models," *Computers and Geotechnics*, vol. 132, Article ID 104017, 2021.

[30] V. Mircevska, M. Nastev, and A. Nanevska, "Seismic slope displacement of tailings dam: a comparative study between modified newmark and Mohr–Coulomb models," *Journal of Earthquake Engineering*, vol. 26, no. 15, pp. 7878–7900, 2022.

[31] Z. Ren, K. Wang, Q.-S. Zhang et al., "Earthquake dynamic response behavior of Xiangchong Valley type tailings impoundment in Yunnan, China," *Journal of Mountain Science*, vol. 15, no. 1, pp. 82–99, 2018.

[32] J. Jin, C. Song, B. Liang, Y. Chen, and M. Su, "Dynamic characteristics of tailings reservoir under seismic load," *Environmental Earth Sciences*, vol. 77, no. 18, 2018.

[33] O. Ledesma, A. Sfriso, and D. Manzanal, "Procedure for assessing the liquefaction vulnerability of tailings dams," *Computers and Geotechnics*, vol. 144, Article ID 104632, 2022.

[34] M. A. Zardari, H. Mattsson, S. Knutsson, M. S. Khalid, M. V. S. Ask, and B. Lund, "Numerical analyses of earthquake induced liquefaction and deformation behaviour of an upstream tailings dam," *Advances in Materials Science and Engineering*, vol. 2017, Article ID 5389308, 12 pages, 2017.

[35] W. Wang, G. Cao, Y. Li et al., "Experimental study of dynamic characteristics of tailings with different reconsolidation degrees after liquefaction," *Frontiers in Earth Science*, vol. 10, pp. 1–11, 2022.